RESEARCH ARTICLE | JANUARY 17 2025

Modeling the fluid dynamics of mitral valve for clinical applications and surgical mitral valve repair

D. Collia ; D. H. Adams; M. G. Trivieri ; Z. A. Fayad ; G. Pedrizzetti ; D. Pandis

Physics of Fluids 37, 011916 (2025)
https://doi.org/10.1063/5.0248930

Physics of Fluids ARTICLE pubs.aip.org/aip/pof

Modeling the fluid dynamics of mitral valve for clinical applications and surgical mitral valve repair

Cite as: Phys. Fluids **37**, 011916 (2025); doi: 10.1063/5.0248930
Submitted: 14 November 2024 · Accepted: 9 December 2024 ·
Published Online: 17 January 2025

D. Collia,[1,2,a] D. H. Adams,[1] M. G. Trivieri,[2,3] Z. A. Fayad,[2] G. Pedrizzetti,[4] and D. Pandis[1]

AFFILIATIONS

[1]Department of Cardiovascular Surgery, Icahn School of Medicine at Mount Sinai, New York, New York, USA
[2]BioMedical Engineering and Imaging Institute, Icahn School of Medicine at Mount Sinai, New York, New York, USA
[3]Cardiovascular Institute, Icahn School of Medicine at Mount Sinai, New York, New York, USA
[4]Department of Engineering and Architecture, University of Trieste, Trieste, Italy

[a]**Author to whom correspondence should be addressed:** dario.collia@mountsinai.org and dar.collia@gmail.com

ABSTRACT

The geometric properties of the mitral valve (MV), the valve controlling the inflow of blood to the left ventricle (LV), is a primary subject of study in clinical cardiology since its movements represent central points for differentiating physiological from pathological conditions. The ability of describing and modeling MV-LV dynamics is fundamental for improving MV repair surgical procedure. The realistic MV modeling is challenging for each individual patient because the mechanical properties of tissues are not accessible noninvasively, making a rigorous fluid–structure interaction approach not easily applicable in a clinical scenario. This study reformulates and extends a dynamic MV model for numerical simulation of LV flow based on diagnostic images recorded during clinical routine and compared it with *in vivo* recordings of the original valve obtained by highly accurate echocardiography which allowed the MV frame-by-frame recording. Results validate the model for clinical application and indicate that the dynamic of the MV during its opening and closure is primarily driven by the flow with negligible contribution from elastic resistance. The numerical model is then employed to provide preliminary analysis of the implications in terms of fluid dynamics of the corrective MV repair surgery. Results confirm that after mitral valve repair the regurgitant volume is drastically reduced, the intracavitary kinematic flow transit across the LV is restored to near-normal pattern but with substantial differences in terms of energetic terms and time course of hemodynamic forces. This study confirms the feasibility of integrating numerical models and clinical imaging technologies for clinical evaluation.

I. INTRODUCTION

The mitral valve (MV) is one of the four cardiac valves located between the left atrium (LA) and the left ventricle (LV). Its principal function is to allow the low-pressure blood from LA to flow to the LV and prevent retrograde backflow when the LV increases its pressure during pumping blood into the circulation. Anatomically, the MV apparatus consists of an incontiguous fibrous ring, called mitral annulus, two leaflets of asymmetric size and the sub-valvular chordal support network connecting the leaflets to the endocardial LV wall tissue.[1] Fluid–structure interaction (FSI) represents a crucial point in the study of MV fluid dynamics as the movement and orientation of the two leaflets is fully driven by the crossing flow and can differentiate a physiological condition from pathological one.[2,3] A variation of the regular flow direction within the ventricle can lead to different a distributions of wall shear stress that, in turn, causes mechanical stresses and adaptation potentially leading to both myocardial fibrosis and inflammation.[4]

The mitral prolapse is the predominant valve disease in the western world. Myxomatous degeneration includes a progressive series of degenerative diseases that expand from fibroelastic deficiency to Barlow syndrome; the latter, has as its main characteristic that of making the leaflets redundant with excessive volume and/or height, determining a retrograde blood flow in the left atrium during mid-late systole, associated with a significant variation in the observed left ventricular flow patterns.[5–7] However, recent studies suggest that non-myxomatous inflammation and myocardial damage occur before the development of hemodynamically significant mitral regurgitation,[8] thus, encouraging further study of valve movement and its influence in different clinical scenarios. The recommended treatment for severe degenerative mitral valve regurgitation is surgical mitral valve repair

(MV_r), the gold standard therapeutic procedure for patients with degenerative mitral valve regurgitation wich follows two fundamental principles: restore a good surface of leaflet coaptation and correct annular dilatation;[9,10] preferred to prosthetic replacement with a biological or mechanical valve due to the superior event-free survival following surgical repair.[10,11]

Literature reports many numerical studies on LV fluid dynamics that are performed using an orifice in valve position simulating a completely open behavior during the diastolic phase and completely closed during the systolic phase, not taking into account the importance of the dynamics of the MV leaflets that were demonstrated to significantly affect the blood flow inside the LV.[12] More recent studies are performed using rigorous FSI models that obey a deformation equation of an elastic material under the action of a given flow-driven pressure difference distribution between the two sides of the leaflets.[13] An approach of this type is perfectly suited for the analysis of prosthetic valves[14] since the properties of the manufacturing materials are known, in principle. However, this rigorous method is not easily transferable to a clinical subjective context, because the elastic or viscoelastic properties of the valvular tissues are not quantifiable *in vivo* at the individual level. Indeed, the mitral leaflets are made up of a non-homogeneous structure with variable thickness, which depends on the clinical state of the valve,[15] and of a non-isotropic fibrous texture near the annulus which becomes looser and thinner as it approaches the trailing edge.[16] In such a clinical context, the possibility of performing computational studies that are patient-oriented, pursuing the so-called "precision medicine," must rely on approaches that exploit the noninvasive information that can be extracted by medical imaging (e.g., Echocardiography, MRI, CT).

In a patient-specific clinical situation, the 3D LV geometry can be obtained with relative accuracy by diagnostic imaging; the limitations of imaging technology, however, do not allow to carefully resolve the details of the MV 3D elements and, particularly, to capture its rapid motion during opening or closure. Typically, the valve can be well visualized in its closed and open positions that last longer; therefore, a model to reproduce the MV dynamics at intermediate positions must be conceived. Along this line, a simplified model for reproducing the dynamics of the valvular leaflets was developed for an ideal MV in the asymptotic condition of leaflets moving within a set of predefined geometric configurations described by a single degree of freedom.[17] The same model was later extended to MV geometry described by an arbitrary number of degrees of freedom and with the set of configurations reconstructed with continuity between the open and closed geometries segmented from medical images.[12] In that model, the movement of the individual leaflets was achieved by a kinematic principle according to which the movement of the leaflets' surface best matches the velocity of the fluid at the valve position. This model was validated with a FSI study in a simple MV[13] and was then successfully employed in a series of theoretical studies.[6,7,18–21] To date, the application of MV modeling to specific patient conditions remains an open challenge as it requires the possibility of model calibration to match patient data and of an assessment of its fidelity. The availability of such models would be of paramount relevance to allow the evaluation of blood flow in correspondence of specific MVs.

With the long-term objective of patient-oriented studies of MV surgery, this study extends the previous MV model for assessing LV fluid dynamics[12] in a way that it fits within the procedure effectively performed in a clinical environment; it introduces the influence of elastic resistance to the MV, adapting a concept previously presented,[22] capable of tuning the valve dynamics with the information effectively available at an individual level. The formulated procedure for patient-specific MV dynamic model is then validated through comparison with the valve excursion measured *in vivo* by high spatial and temporal resolution echocardiography that allows frame-by-frame recording of the MV.

The MV model is then employed to explore the properties of LV fluid dynamics before and after the MV_r procedure in a few subjects with the objective to provide information on the functional problems of the diseased valve and on the quality of blood flow pattern after repair.

II. METHODS AND MODELS

A. Imaging and *in vivo* geometry

The geometry of the LV chamber and of the MV were extracted from 3D-transesophageal echocardiography (TEE) or 3D-transthoracic echocardiography (TTE) as follows. The LV moving boundaries are obtained by a semi-automatic procedure through a software certified for clinical use (4D LV-Analysis; TomTec Imaging Systems GmbH, Unterschleissheim, Germany) that also identifies the size and location of the valves. The geometry of the MV, at the inlet of LV, was extracted through a companion software (4D MV-Assessment; TomTec Imaging Systems GmbH, Unterschleissheim, Germany).

The clinical images used were registered with TTE for 5 normal cases and with TEE for 5 MV_r patients pre-surgery and post-surgery, for a total of 15 case records. TTE is the gold standard method used for routine cardiovascular examinations[23–26] and allows to obtain normal cases that would otherwise not be possible to obtain with TEE due to the invasiveness of the latter. The LV geometry evaluated immediately pre-implant was used for both the pre- and post-MV_r as the main geometric and volumetric properties (end-diastolic volume EDV, end-systolic volume ESV) do not vary appreciably with surgery. This approach allows focusing on the differences induced by MV surgery only and reduces confounding factors imputable to minor variability during image recording and processing.

However, 3D echocardiography has many limitations, including the difficulty of obtaining quality images at a high frame rate. An increase in the frame rate can lead to stitching and gating artifact errors[27] which do not allow the valve movement to be correctly detected. These difficulties occur during both TTE and TEE examinations and are more frequent in patients than in healthy subjects.[28] Eventually, we were able to reliably record the frame-to-frame MV motion (MV_{Ftf}) in two normal subjects; in all others, the MV geometry was recorded in the fully open and fully closed configurations only as shown in Fig. 1. Indeed, in all MV_r patients it is extremely difficult to identify the valve excursion of all frames as the TEE recording is intra-surgical, with the risk of the presence of artifacts due to instruments or stitching threads. The two MV_{Ftf} cases were used for the in-vivo experimental verification of the results about MV dynamics obtained with the model (MV_{Dyn}). Recording details are reported in Table I including the prolapse type for patients, according to the Carpentier method.[9] Figure 2 shows the MV 3D geometries of the normal, pre- and post-surgical MV_r listed in Table I.

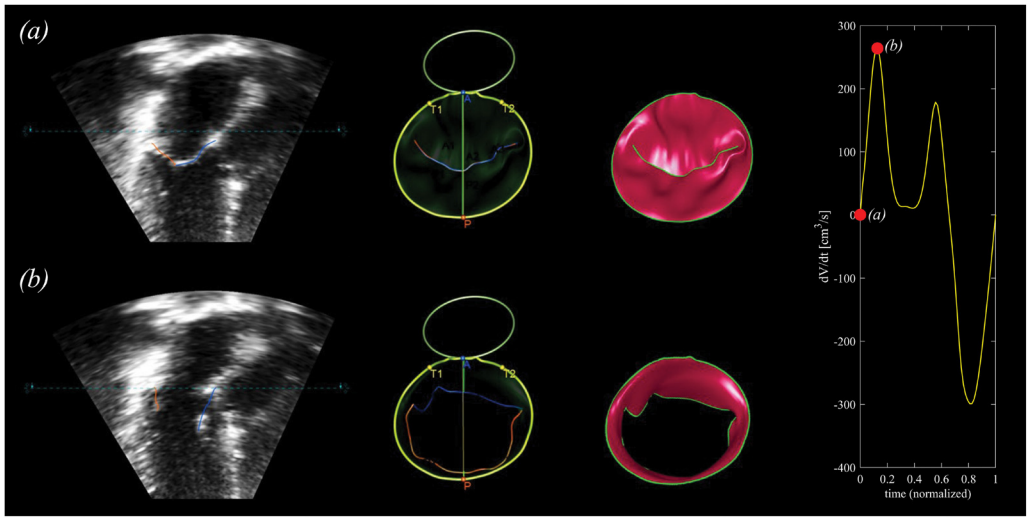

FIG. 1. Graphical visualization of the MV fully open and fully closed configurations of the Normal 1 obtained with TomTec 4D-Assessment and reconstructed in 3D with MATLAB. On the right side is showed the dV/dt curve (yellow color) and two points (red color) indicating respectively the (a) fully closed and (b) fully open of the MV configuration.

The LV-MV geometric model is obtained by segmenting the same 3D echocardiographic image in order to obtain the same geometric and parametric coordinates of the specific patient case both in terms of size and orientation. This methodology allows to obtain the mitral plane (segmented with TomTec 4D LV-Analysis) consistent with the MV (segmented with TomTec 4D-Assessment), and therefore, a structurally complete geometry. Subsequently the valve is attached to the mitral plane of the ventricle in post-processing, with MATLAB software (R2024b) (MathWorks, Natick, MA), aligning MV to LV in terms of points and orientation. This allows to preserve the frame-by-frame MV kinematics that is also exploited by the MV_{Dyn} model as it follows the same principle starting from the fully closed and fully open MV configuration as described above.

Mathematically, the valve is represented as a membrane of zero thickness whose geometry at the various instants of time is described by the position vector $\mathbf{X}_{MV}(\vartheta, s, t)$, where (ϑ, s) are two (arbitrary) parametric coordinates describing the valve around the circumference and from the annulus, $s = 0$, to the trailing edge, $s = 1$, and t is the time. In general, the valve geometry can be recorded at few instants only during its motion, typically in fully open and fully close configurations. In the present model, the principle is to let the geometry extend between the available limiting positions and reconstruct the intermediate geometric configurations by considering the two edges as if they move independently, each describing one degree of freedom associated with the opening angle, say $\varphi_1(t)$ and $\varphi_2(t)$, for the anterior and posterior leaflets, respectively. The valve geometry in a generic configuration is, therefore, described by its coordinates $\mathbf{X}_{MV}(\vartheta, s, \varphi_1, \varphi_2)$, which represent a two-dimensional set of geometries associated with the two degrees of opening of the leaflets. This allows the two MV leaflets to assume different degrees of opening, respectively for φ_1 and φ_2, starting from 0 (completely closed) up to $\frac{\pi}{2}$ (fully open). This set of geometries is estimated by interpolation

TABLE I. Echo characteristics of normal, pre- and post-MV_r cases in terms of number of frame, registration type, prolapse type (pre-MV_r), and saving type.

Case	No.of frames	Registration type	Prolapse type (pre MV_r)	MVrecorded geometry
Normal 1	23	TTE	…	frame-to-frame
Normal 2	23	TTE	…	frame-to-frame
Normal 3	21	TTE	…	open/closed
Normal 4	20	TTE	…	open/closed
Normal 5	17	TTE	…	open/closed
MV_r 1	42	TEE	P2	open/closed
MV_r 2	32	TEE	P2	open/closed
MV_r 3	32	TEE	P2	open/closed
MV_r 4	14	TEE	P3	open/closed
MV_r 5	11	TEE	P1-P3	open/closed

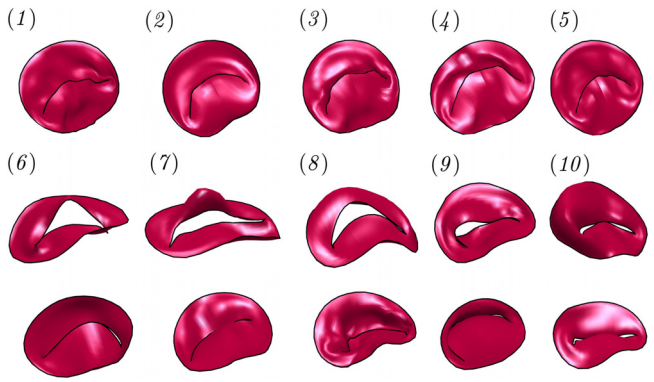

FIG. 2. Geometrical representation of the MV geometries in normal (1–5), pre- and post-surgical MV_r (6–10) configuration.

TABLE II. Clinical data of normal, pre- and post-surgical MV_r cases in terms of average and standard deviation. *EDV* = End Diastolic Volume, *ESV* = End Systolic Volume, *SV* = Stroke Volume, *EF* = Ejection Fraction. The values are reported as mean ± SD.

Case	EDV (cm^3)	EDV (cm^3)	SV (cm^3)	EF (%)
Normal	96 ± 9	39 ± 4	57 ± 5	59 ± 2
MV_r	106 ± 14	50 ± 5	56 ± 10	53 ± 3

between $\mathbf{X}_{MV}(\vartheta, s, 0, 0)$ and $\mathbf{X}_{MV}\left(\vartheta, s, \frac{\pi}{2}, \frac{\pi}{2}\right)$ configurations as previously described.[12]

This approach neglects both the influence of the tendinous chords, whose effect is replaced by preventing the valve from opening toward the atrium, and the possible impact of the leaflets on the surrounding tissues, which is simply predicted using their original fully open and fully closed configurations. Conversely, studies in the Ref. 29 have shown that the only advantage of including the tendinous chords in a numerical model is precisely that of avoiding the use of *ad hoc* kinematic constraints to imitate their effect, a major disadvantage instead is represented by the increase in computational load due to the presence of additional structures that, being thin filaments, are very demanding for the spatial resolution requirements; since nothing changes from the fluid dynamics point of view, they should be inserted only in the case of extreme necessity.

The aortic valve (AV) at the outlet is then modeled by a simple binary behavior, fully open or fully closed. The positioning of the valves in the ventricular geometry is specified by the ventricular registration itself and does not require explicit registration.

The basic functional data of the population analyzed here is reported in Table II in terms of mean ± SD. Examples of complete 3D geometry relative to Normal 1, pre-MV_r 4, and post-MV_r 5 cases are shown in Fig. 3.

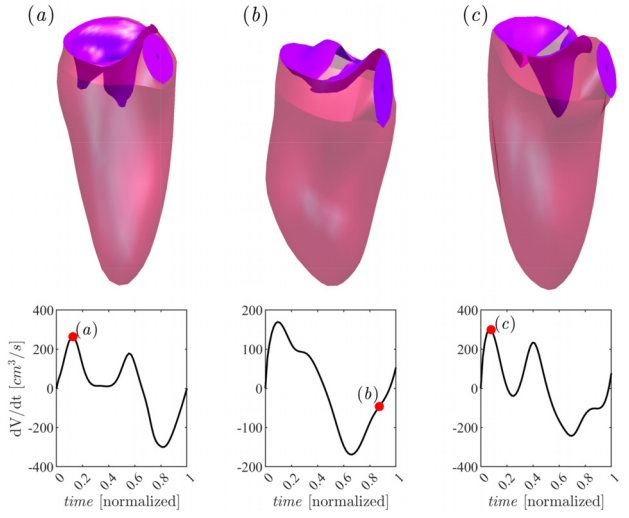

FIG. 3. Complete geometry of the Normal 1 (a) in E-wave peak position, pre-MV_r 4 (b) in late systolic phase position and post-MV_r 5 (c) in E-wave peak position; In the below section is showed the flow rate curve during entire cardiac cycle of the, respectively, cases.

B. Fluid dynamics

The intraventricular fluid dynamics is evaluated by numerical solution of the Navier–Stokes and continuity equations

$$\frac{\partial \boldsymbol{v}}{\partial t} + \boldsymbol{v} \cdot \nabla \boldsymbol{v} = -\nabla p + \nu \nabla^2 \boldsymbol{v}, \tag{1}$$

$$\nabla \cdot \boldsymbol{v} = 0; \tag{2}$$

where $\boldsymbol{v}(t, \boldsymbol{x})$ is the velocity vector field, $p(t, \boldsymbol{x})$ is the kinematic pressure field, and ν is the kinematic viscosity (assumed 0.04 cm^2/s).

The numerical method was described and validated for cardiac flow applications in a previous methodological study;[12] the main points are summarized below. The solution is achieved by the immersed boundary method (IBM) in a bi-periodic Cartesian domain; time advancement is achieved using a fractional step method in combination with a third-order Runge–Kutta explicit scheme, and no-slip boundary conditions are set on the moving immersed boundaries that comprise the ventricle geometry and valve surface. The movement of the LV boundary is imposed to be the one extracted by clinical images, the movement of the MV is obtained during evolution by the model described below in C. The aortic valve is modeled as a simple orifice with a flat surface that is either open or closed. Aorta is considered open when the MV is closed and the normal velocity, averaged over the position of the AV surface, is directed outwards.

C. Mitral valve dynamics

The basic concept of MV dynamics is described in Ref. 12 and it is briefly recalled here. The dynamics of the valve leaflets is first modeled in the limiting condition of no explicit resistance other than respecting the set of geometry obtained from medical imaging $\mathbf{X}_{MV}(\vartheta, s, \varphi_1, \varphi_2)$, and therefore, given by the time evolution of the two degrees of freedom ($\varphi_1(t)$ and $\varphi_2(t)$) describing the opening of the two leaflets. Individual leaflets' movement was obtained by the kinematic condition that the motion of the leaflet surface must match the velocity of the fluid at the same position. This is imposed in the least squares sense, in integral form over each individual leaflet, and gives rise to the system of dynamic equation for the advancement of each leaflet opening angle. In the present case of 2 degree of freedom, this procedure results in a 2 × 2 system of linear equations

$$M_{ij} \frac{d\varphi_j}{dt} = f_i. \tag{3}$$

for the two unknowns $\frac{d\varphi_1}{dt}, \frac{d\varphi_2}{dt}$. The matrix elements in (3)

$$M_{ij} = \int\int_{A_v} \left(\frac{\partial \mathbf{X}_{MV}}{\partial \varphi_i} \cdot \boldsymbol{n}\right)\left(\frac{\partial \mathbf{X}_{MV}}{\partial \varphi_j} \cdot \boldsymbol{n}\right) dA, \tag{4}$$

represents the mutual influence of the different degrees of freedom, and "$\boldsymbol{n}$" is the normal to the valvular surface. The symmetric matrix (4) is diagonally dominant and ensures that the system is well conditioned. The forcing element

$$f_i = \int\int_{A_v} (\boldsymbol{v} \cdot \boldsymbol{n})\left(\frac{\partial \mathbf{X}_{MV}}{\partial \varphi_i} \cdot \boldsymbol{n}\right) dA, \tag{5}$$

represents the kinematic interaction with the fluid. More details on the derivation of this model were previously reported in Ref. 12 for an

arbitrary number of degrees of freedom. The system (3), whose solution gives $\frac{d\varphi_i}{dt}$, is evaluated in parallel to the Navier–Stokes Eq. (1), that gives $\frac{d\mathbf{v}}{dt}$, during the substeps of the Runge–Kutta time advancement of fluid velocity and valve position.

Equations (3) are obtained under the assumption that the valve moves with the flow with no additional resistance other than the constraint of maintaining the geometry described by a limited number of degrees of freedom. Therefore, the model present no adjustable parameters to account for more or less elastic tissue conditions. The presence of a non-negligible tissue elasticity gives rise to the reduction of the valvular opening rate due to an elastic recall force that can be accounted by a formal modification to expression (3) as

$$M_{ij}\left(\frac{d\varphi_j}{dt} - CF_j(\boldsymbol{\varphi})\right) = f_i \tag{6}$$

where $F_i(\varphi_1, \varphi_2)$ is a dimensionless vector function that represents the effects of elasticity, the coefficient C is a global characteristic of tissue stiffness, it has the dimension of the inverse of time which is proportional to the time of valvular closure in the absence of force.[22] The function $F_i(\varphi_1, \varphi_2)$ describes the elastic force and can be expressed in terms of a dimensionless strain-energy function for the valve tissue $W(\varphi_1, \varphi_2)$

$$F_i = \frac{dW}{d\varphi_i}. \tag{7}$$

The strain-energy function is evaluated from the deformation of the valve geometry, described by the coordinates $\mathbf{X} = \mathbf{X}_{MV}(\varphi_1, \varphi_2)$, relative to the reference undeformed state $\mathbf{X}_0 = \mathbf{X}_{MV}(0, 0)$. The transformation from $\mathbf{X}_0$ to X is described by the deformation gradient $\mathscr{F}$

$$\mathscr{F}_{ij} = \frac{\partial X_i}{\partial X_{0j}}., \tag{8}$$

with i and j indicate the local tangent directions on the two-dimensional valvular surface and take value 1, 2. The transformation $\mathscr{F}$ can be separated through the polar decomposition as

$$\mathscr{F} = \mathscr{R}\,\mathscr{U}, \tag{9}$$

where $\mathscr{R}$ is the rotation matrix, and $\mathscr{U}$ is the *right stretch tensor* that contains the information about deformation.[30] The strain-energy function[31] is described here with its simplest expression of a neo-Hookian hyperelastic material as

$$W = \frac{1}{A_{MV}} \iint_{A_{MV}} (I - 3)\, dA, \tag{10}$$

where $I = \lambda_1^2 + \lambda_2^2 + \lambda_3^2 - 3$ is the first invariant of the deformation tensor, the two values $\lambda_1(\varphi_1, \varphi_2)$ and $\lambda_2(\varphi_1, \varphi_2)$ are the 2 eigenvalues of the right stretch tensor $\mathscr{U}$, such that $\lambda_i(0, 0) = 1$. The third eigenvalue is evaluated by tissue incompressibility condition $\lambda_1\lambda_2\lambda_3 = 1$. The deformation tensor is evaluated on the individual elements describing the MV geometry, and the surface integral is performed with reference to the undeformed configuration.[21] Given the complete independence of the two degrees of freedom in the present MV geometric model, the eventual elastic functions are also separated as $F_1(\varphi_1)$ and $F_2(\varphi_2)$; the two functions are reported in Fig. 4. The average value of the two components F_1 and F_2 is in line with the study by Celotto *et al.*[22] with one degree of freedom. The shorter leaflet reaches its maximum opening peak ($\varphi_2 = \pi/2$) with less elastic resistance in qualitative agreement with the observation that it opens with greater speed than the other that, being longer, opens with greater deformation.[13,32]

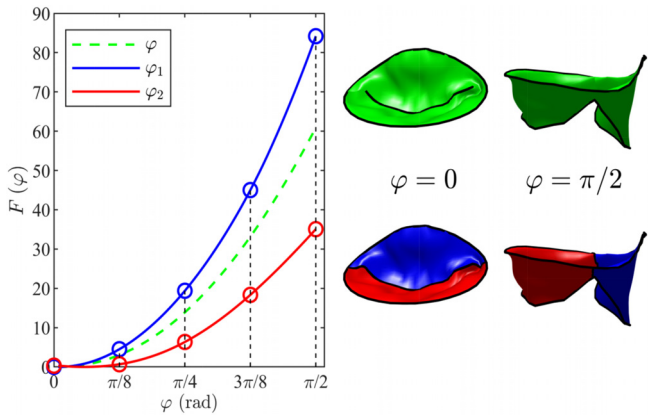

FIG. 4. Graphical representation of the function $F(\boldsymbol{\varphi})$ (left side); geometrical representation of the MV in open and closed configuration (right side), respectively, for complete MV (φ) in green color, anterior leaflet (φ_1) in blue color and posterior leaflet (φ_2) in red color.

III. FLOW QUANTIFICATION METHODS

A. Effective orifice area

The effective orifice area (A_{eff}) represents the area of the effectively open section between the MV trailing edges. It is a physical measure, independent from the model used, and can be employed to compare the MV dynamics between different models or with measurements. It is calculated from the MV geometry

$$A_{eff}(t) = \int_0^L \int_{\mathbf{X}_{e_{ant}}}^{\mathbf{X}_{e_{post}}} ds\, dL, \tag{11}$$

where $\mathbf{X}_{e_{ant}}$ and $\mathbf{X}_{e_{post}}$ are the facing trailing edges of the anterior and posterior leaflets, respectively. In the present model, $\mathbf{X}_{e_{ant}} = \mathbf{X}_{MV}(\vartheta, 1)$ with ϑ spanning from 0 to π, and $\mathbf{X}_{e_{post}} = \mathbf{X}_{MV}(\vartheta, 1)$ with ϑ spanning from 2π backward to π. The external integration is carried along the length L of a curve defined by the midpoint between the two facing edges, at each such position the internal integral computes the distance between the facing edges.

Similarly, it is possible to compute the flow rate of the fluid effectively crossing the MV by

$$Q_{MV}(t) = -\int_0^L \int_{\mathbf{X}_{e_{ant}}}^{\mathbf{X}_{e_{post}}} \boldsymbol{v}_{rel} \cdot \boldsymbol{n}\, ds\, dL = -\int_{A_{eff}} \boldsymbol{v}_{rel} \cdot \boldsymbol{n}\, dA, \tag{12}$$

where $\boldsymbol{v}_{rel}$ is the relative velocity of fluid (the velocity of the fluid minus the velocity of the ideal surface at that point) and the minus sign follows from the fact that $\boldsymbol{n}$ is the outward unit normal vector.

B. Flow transit analysis

The identification of blood transport and mixing inside the LV is a useful marker to analyze blood residence and wash-out properties. This is used in several clinical studies because an inefficient LV cannot

properly expel the correct amount of stagnant blood during its systolic phase and this increases the risk of thrombus formation.

Following the consolidated literature in cardiology,[33,34] it is common to evaluate the flow transit by dividing the EDV into 4 subvolumes

$$EDV = V_{direct} + V_{retained} + V_{delayed} + V_{residual}, \tag{13}$$

where V_{direct} is the volume of blood that entered during diastole and transits directly to the aortic outlet during systole, thus residing less than one heartbeat in the LV. $V_{retained}$ is the part that entered during diastole that is not ejected during the following systole while $V_{delayed}$ was already present in the LV at the beginning of diastole and is then ejected during the following systole. Finally, $V_{residual}$ was present in the LV before the beginning of diastole and remains in the chamber after the end of systole.

In formulas, the stroke volume $SV = EDV - ESV$ of blood entering during diastole, is composed of

$$SV = V_{direct} + V_{retained}, \tag{14}$$

the quantity of blood found in the LV at the end of the systolic ejection is given by

$$ESV = V_{retained} + V_{residual}, \tag{15}$$

whereas the systolic outflow volume is

$$SV = V_{direct} + V_{delayed} + V_{reg}, \tag{16}$$

where V_{reg} is the volume regurgitated in the atrium when the MV is insufficient, which is measured directly from time integration of the flow rate (12) crossing the MV during systole[5]

$$V_{reg} = \int_{T_{sys}} Q_{MV}(t)\, dt, \tag{17}$$

where T_{sys} is the systolic time interval.

The analysis of blood transport is performed by solving the transport-diffusion equation for a passive scalar representing a marked volume of blood itself

$$\frac{\partial C}{\partial t} + \nabla \cdot (\boldsymbol{v} C) = \nu \nabla^2 C, \tag{18}$$

where $\boldsymbol{v}(\boldsymbol{x}, t)$ is the known divergence-free velocity field, $C(\boldsymbol{x}, t)$ is the concentration of marked blood elements. Equation (18) is solved in parallel to the Navier–Stokes Eq. (1) starting from the initial condition $C(\boldsymbol{x}, 0) = 1$ in the interior of the ventricle at beginning of diastole. Therefore, the average concentration starts from a unitary value and decreases progressively every heartbeat when the marked particles are replaced by fresh blood ($C = 0$) entered from the atrium. This method also allows us to differentiate the composition of fresh and old blood entering and exiting the left ventricle and regurgitating into the atrium.[2,5] In particular, according to (15), the residual volume is composed of the labeled blood that is found in the LV chamber at the end of the next systole

$$V_{residual} = \int_{ESV} C\, dV. \tag{19}$$

Once then $V_{residual}$ (and V_{reg} in the presence of mitral insufficiency) are known, its possible to identify all contributions through the linear relationships of the Eqs. (13)–(16).

The knowledge of the concentration field C allows to differentiate fresh and old blood flow rate across the valve using an extension of (12)

$$Q_C(t) = -\int_{A_{eff}} \boldsymbol{v}_{rel} \cdot \boldsymbol{n}\, C\, dA. \tag{20}$$

and the corresponding volumes are then obtained as the time integral of the flow rate in the reference period (i.e., systole or diastole), like in (17) which can be either the forward volume or the regurgitated back flow.[18]

C. Kinetic energy and dissipation rate

The kinetic energy (KE) of the blood reflects a fundamental component of the work performed by the LV[35] and it is calculated as follows

$$KE(t) = \frac{\rho}{2} \int_V |\boldsymbol{v}|^2\, dV, \tag{21}$$

where $V(t)$ is the ventricular volume and ρ the blood density.

The KE dissipation rate provides a measure of the efficiency of blood flow and it is an indicator of ventricular function.[36] It is expressed as follows:

$$D(t) = \rho \nu \int_V S_{ij} \frac{\partial v_i}{\partial x_j}\, dV, \tag{22}$$

where $\mathbf{S}$ is the rate of deformation tensor and ν the kinematic viscosity. We intentionally kept these parameters in their dimensional form to serve as reference for the cardiology literature because there is an increase in clinical studies reporting dissipation evaluated from medical imaging.[36–40] However, the existing imaging technologies present differences in spatial resolutions and usually insufficient to cover all dissipation scales; therefore, the presented values may not be accurate or comparable one another.

D. Vorticity and vortex formation time

The formation of the vortex and its orientation within the LV influence the correct course of the flow throughout the cardiac cycle until its expulsion.[41] The average vorticity inside the ventricle, made dimensionless with the heartbeat period T, is evaluated by

$$\bar{\omega} = \frac{T}{V} \int_V \omega\, dV, \tag{23}$$

where $\omega(\boldsymbol{x}, t) = |\nabla \times \boldsymbol{v}|$ is the modulus of the vorticity vector field.

The vortex formation time (VFT) is an important dimensionless parameter used for the evaluation of LV function;[42] this dimensionless parameter is computed as

$$VFT = \int_{T_E} \frac{v_{MV}(t)}{d(t)}\, dt, \tag{24}$$

where $v_{MV} = \frac{Q_{MV}}{A_{eff}}$ is the mean velocity across the MV orifice, $d = \sqrt{\frac{4}{\pi} A_{eff}}$ the average MV orifice diameter, and T_E is the diastolic E-wave period. This parameter measures the quality of the vortex formation process and optimal LV filling. Studies present in literature

have shown that the optimal range is $3 \leq VFT \leq 4$, although a value up to 5 is also considered acceptable.[43] High values are associated with the breakdown of the forming vortex and turbulence, while lower values correspond to suboptimal propulsion.[44]

E. Hemodynamic forces

The forces exchanged between blood and the surrounding tissues have special relevance in ventricular function, in particular flow-driven forces were demonstrated to modulate the morphogenesis of embryonic hearts[45] and pathologies in adult hearts.[46] The hemodynamic force (HDF), which depends on major features of intraventricular flow, represents the total force exchanged between blood and tissue. In integral terms, the force acting on a volume $V(t)$ of fluid is given by the gradient of the pressure field, $p(\boldsymbol{x}, t)$, where $\boldsymbol{x}$ is the 3D space coordinate and t is time, integrated on that volume, plus the viscous stresses, $\tau(\boldsymbol{x}, t)$ integrated over the volume boundary $S(t)$

$$\boldsymbol{F}(t) = \int_{S(t)} \tau dS - \int_{V(t)} \nabla p \, dV. \tag{25}$$

The expression (25) can be rewritten in terms of fluid velocity vector field, $\boldsymbol{v}(\boldsymbol{x}, t)$, by using the law for conservation of momentum [e.g., the Navier–Stokes Eq. (1)]

$$\boldsymbol{F}(t) = \rho \int_{V(t)} \left(\frac{\partial \boldsymbol{v}}{\partial t} + \boldsymbol{v} \cdot \nabla \boldsymbol{v} \right) dV, \tag{26}$$

where ρ is the fluid density. The volume integral (26) can be computed from the results of the fluid dynamic simulation; however, it can also be rewritten, with the aid of the Gauss theorem, in the simpler form of a surface integral and evaluated from the dynamics of the LV boundary and the exchange of momentum across the mitral and aortic orifices[47]

$$\boldsymbol{F}(t) = \rho \int_{S(t)} \left[\boldsymbol{x} \left(\frac{\partial \boldsymbol{v}}{\partial t} \cdot \boldsymbol{n} \right) + \boldsymbol{v}(\boldsymbol{v} \cdot \boldsymbol{n}) \right] dS. \tag{27}$$

where $\boldsymbol{n}$ is the outward unit normal vector. In this study, the global force vector is normalized with the LV volume to remove dependence on LV size, it is then divided by density and gravity acceleration g, to have it expressed in dimensionless form $\frac{\boldsymbol{F}(t)}{\rho g V(t)}$.

IV. VERIFICATION AND VALIDATION

A. Numerical verification

The influence of numerical parameters on the numerical results model was analyzed in previous studies for similar conditions.[12,19] A grid refinement analysis is performed here on a bi-periodic domain of size $10 \times 10 \times 12$ cm that was previously verified to ensure absence of confinement effects, results are reported in correspondence of three different numerical resolutions ranging from a basic grid $160 \times 160 \times 192$ points and 4096 time-steps in one heartbeat, to a refined grid $192 \times 192 \times 224$ points and 6144 time steps, and a further refined grid $224 \times 224 \times 256$ points and 8192 time-steps. The case used for this purpose is the Normal 1. All simulations started from irrotational flow conditions and were performed for at least 3 heartbeats. Here and below, results are reported for the last complete heartbeat.

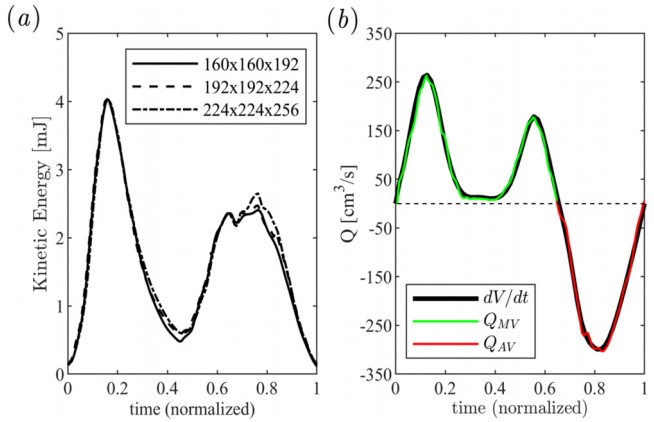

FIG. 5. (a) Kinetic energy inside the LV of the Normal 1 evaluated with different numerical resolution. The continuous line corresponds to a grid made up of $160 \times 160 \times 192$ points; dashed line corresponds to a grid made up of $192 \times 192 \times 224$ points; dash-dot line corresponds to a grid made up of $224 \times 224 \times 256$ points. (b) flow balance: dV/dt (dark line), Q_{MV} is the mitral inflow (green line), Q_{AV} is the aortic outflow (red line).

Figure 5(a) shows the results in terms of KE contained inside the LV as computed with the three different resolutions. The KE shows a very similar common behavior for the different resolutions, with the exception of the periods about $t \simeq 0, 48$ and $(t \simeq 0, 78)$. These differences are imputable to minor changes in the valvular motion during the period of low filling flow (diastasis) and in the transition from MV closure to early systole.

A point requiring special care when using the immersed boundary method is the lack of a mathematical rigorous argument guaranteeing the impermeability boundary condition on the immersed elements.[48] It is, therefore, good practice to verify the absence of leakage across the immersed boundaries. To this aim, Fig. 5(b) compares the flow rate corresponding to the imposed volumetric variation (dV/dt, black line) with the inflow flow rate across the mitral valve (Q_{MV}, green line), computed by Eq. (12), and aortic outflow (Q_{AV}, red line), calculated with the same equation simplified by the absence of leaflets. Results are reported for the intermediate grid, the similarity between the curves confirms the absence of leakage across the boundary, this result is also confirmed numerically through the comparison between the stroke volume obtained from the clinical data (64 cm^3)), that coincides with both the mitral inflow volume and aortic outflow volume evaluated by the time integral of the green and red curves, respectively. Based on this analysis, the present study used the most refined grid made of $224 \times 224 \times 256$ points.

B. Experimental validation

The performance of the MV model was verified by comparing the numerical simulation using the prescribed motion of the valve measured *in vivo*, MV_{Ptf}, with five simulations with the model of MV dynamics, MV_{Dyn}, in correspondence of different values of the elastic parameter $C = -1, 0, 0.2, 0.6, 1\ s^{-1}$. The case with negative C, that corresponds to a negative elasticity giving an elastic recall away from closed configuration, was included to integrate the verification of model robustness although its physical counterpart is uncertain. The

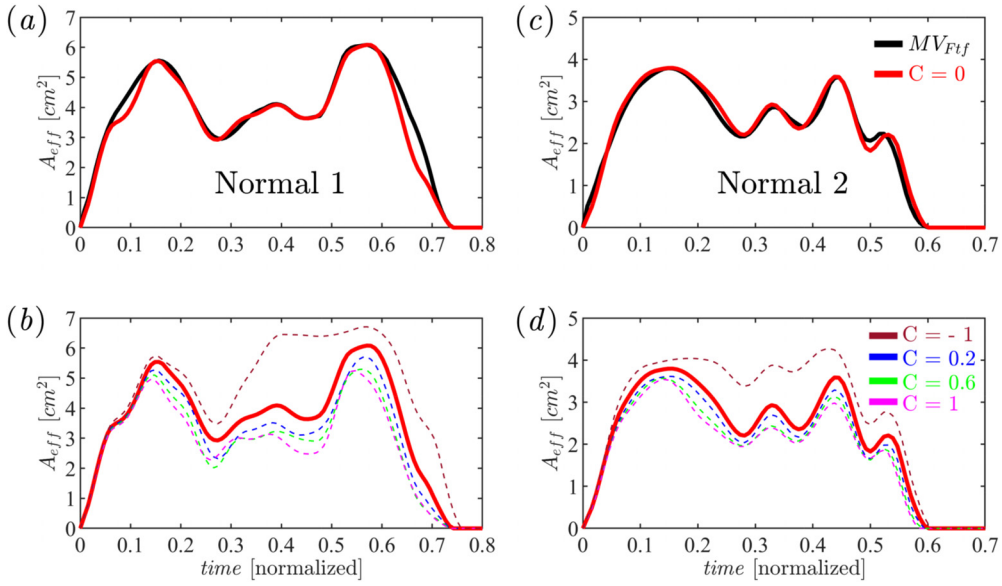

FIG. 6. Comparing of Normal 1 and Normal 2 A_{eff} excursion. (a) and (c) MV_{Ftf} vs MV_{Dyn} with C = 0; (b) and (d) MV_{Dyn} with different value of C. In (b) and (d) label is reported for reference the case with C = 0, respectively, for Normal 1 and Normal 2.

analysis is performed for the two cases, Normal 1 and Normal 2, where the frame-to-frame MV recording was available, for a total of 12 numerical simulations.

The comparison is first performed in terms of the time profile of valve opening at the trailing edge (A_{eff}) computed with Eq. (11). Figures 6(a) and 6(c) show the similar trend of MV_{Ftf} and MV_{Dyn} results obtained in the absence of elastic recall, $C = 0$. An increase in the value of C, Figs. 6(b) and 6(d), gives rise to a valve movement that is similar to the case $C = 0$ during the impulsive opening phase, up to approximately $t \sim 0.13$ in Normal 1 and $t \sim 0.8$ in Normal 2. Subsequently the direct action of the flow is reduced and the MV is subjected to the elastic recall that reduces valvular opening and, as C increases, reduces the valve excursion. The negative value ($C = -1s^{-1}$) confirms the behavior of the model that, in this specific case, tends to open faster and offer an elastic resistance to closure.

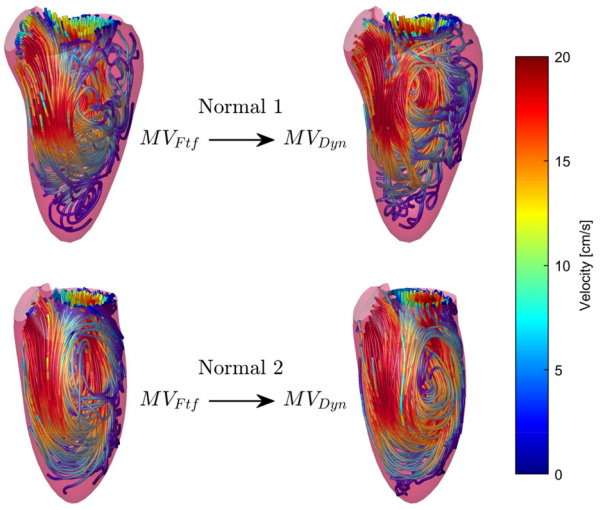

FIG. 7. Comparison of MV_{Ftf} and MV_{Dyn}, respectively, for Normal 1 and Normal 2 through the streamlines of the steady-streaming (heartbeat-average) flow. Streamlines are colored by velocity magnitude.

These results confirm that the most accurate modeling of the observed valvular movement is obtained by setting $C = 0$. This means that the dynamics of the valve are essentially driven by the flow, and elastic resistance gives a negligible contribution to its motion. Conversely, the mechanical properties of the tissue dictate the shape, the geometry of the valve particularly in the state of maximum opening that is recorded from diagnostic images. Based on these results, the subsequent evaluations and further comparisons are performed in correspondence of $C = 0$.

The valve dynamics affects the fluid dynamics inside the LV chamber, in order to allow for a comparison of the three-dimensional velocity field a fluid dynamics simulation was performed without MV model and directly imposing the instantaneous time-varying MV geometry as recorded *in vivo* and interpolated to the high time-resolution required by the simulation. The numerical parameters were identical and comparison was performed through the steady-streaming (or heartbeat-averaged) flow pattern, which is shown in Fig. 7 in terms of streamlines where care is taken to use an identical set of starting points for their evaluation. In both cases, the flow entering from the MV into the LV develops a rotary motion that occupies the entire cardiac chamber and redirects the fluid toward the outlet for subsequent expulsion. A regular LV flow pattern is allowed by its nearly ellipsoidal geometry with the presence of an approximate symmetry plane (the $x - z$ plane) containing the inflow, outflow, and apex[21] where the characteristic and influence of the MV plays a fundamental role.[18,49,50]

These results further confirm that the present MV model well reproduces the valvular motion observed *in vivo*; this also tells that, once the geometry is properly extracted by images, MV dynamics is primarily driven by the flow, i.e., by LV volume rate curve.

V. EVALUATION PRE- AND POST-MV REPAIR

A. Flow patterns

In this section, we apply the model described in Secs. II–IV to evaluate the modifications induced by *MVr* in the five clinical cases listed in Table I to start understanding the impact of *MVr* to the resulting flow pattern.

The flow field in normal conditions was previously described in numerous studies.[12,51,52] At the peak of diastolic filling, it features the formation of a typical asymmetric vortex ring as shown in Fig. 8(a) for the Normal 1 taken as example. Differently, in the pre-repair condition shown in Fig. 8(b) for patient MV_r 1, flow presents an entry jet that deviates posteriorly into the LV with an intense shear to the wall and rapid dissipation of the vortex ring. This condition occurs, with minor differences, in all pathological cases.[5–7] After MV_r, Fig. 8(c), the mitral jet is more compact and directed to the center of the LV, the vortex is smaller and more regular in comparison to the corresponding pre-surgery condition, which is probably a consequence of the MV area reduction due to repair[10,53,54] together with a reduction in valve opening which however did not occur in all cases analyzed.

The overall fluid dynamic pattern during the heart cycle can be qualitatively described by the steady-streaming (or heartbeat-averaged) fields, which are shown in Fig. 8 (d, e, f) in terms of streamlines. In the normal cases [Fig. 8(d)] the flow entering the compact LV geometry develops a rotational movement that occupies the entire chamber, this rotation effectively redirects the fluid toward the outflow for subsequent expulsion.[21] In the pre-MV_r case [Fig. 8(e)] the flow follows a path along the posterior wall up to the apex and then partly goes up toward the aorta for ejection and partly follows a circular motion in the center of the LV and returns to the MV for subsequent regurgitation into the atrium. After repair [Fig. 8(f)], the high-velocity jet propagates deeper into the LV chamber and the directionality of the flow is overall comparable with the normal cases; although, sometimes, the deeper jet reaches the apex where the vortex ring can give rise to a pattern more disturbed than in physiological conditions.[55] This new flow redirection after MV_r shows a clear improvement in left ventricular function in terms of VFT, recovering values comparable to normal cases from the pre-operative ones that were significantly lower testifying to the presence of suboptimal diastolic filling despite the normal EF (average VFT value: 3.8 vs 1.5 vs 3.5, respectively, for normal, pre-MV_r and post-MV_r). The recovery in terms of vortex formation time is a diastolic property that is attributable only to restoration of the MV geometry, given that the volumetric values of the LV do not vary significantly between pre- and post-repair, and the correction of regurgitation pertains to systole.

The comparison between pre- and post-MV_r is reported in Fig. 9 in terms of global properties. Results are averaged over the present small population and the curve corresponding to normal cases is reported as a reference. For consistency when computing the averages, the timescale has been normalized to a common end-systolic and end-diastolic instants (here and in Fig. 10 below). Figure 9(a) shows that

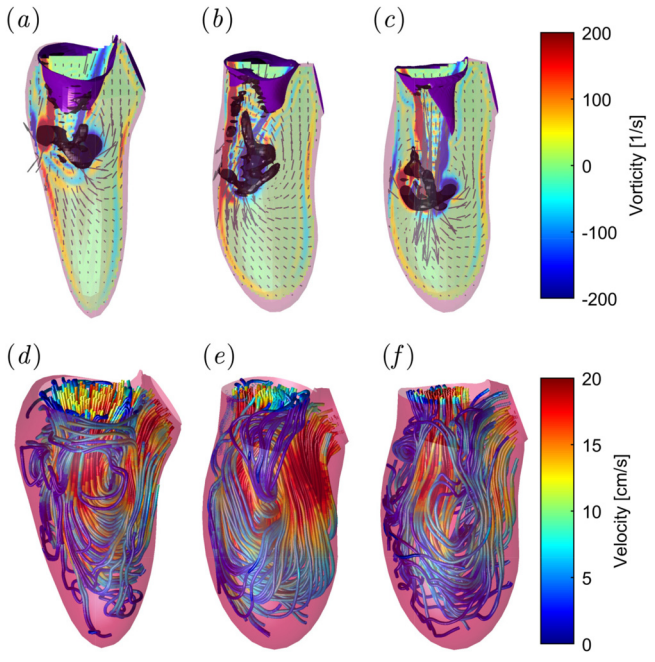

FIG. 8. Upper side: Diastolic flow field at peak E-wave of Normal 1(a), pre-MV_r 1(b) and post-MV_r 1(c). The vorticity is shown by red to blue color from –200 to 200 units; the three-dimensional black surfaces represents one iso-surface of the λ_2 parameter. Lower side: Streamlines of the steady-streaming (heartbeat-average) flow for (d) normal, (e) pre-MV_r, and (f) post-MV_r. Streamlines are colored by velocity magnitude.

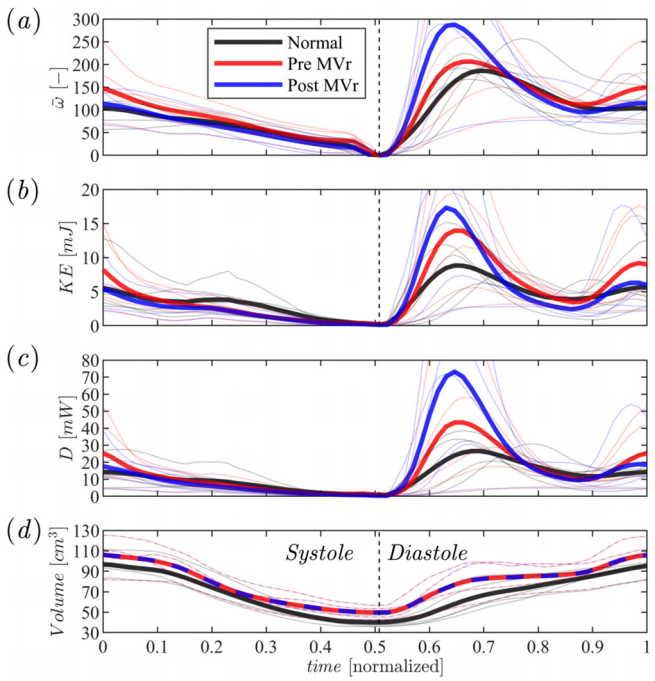

FIG. 9. Graphical representation of the averaged vorticity (a), kinetic energy (b), energy dissipation rate (c), and volume (d) reported at the bottom for timing reference. Each curve represents the average computed from the cases of each group: normal (black lines) pre-MV_r (red), and post-MV_r (blue).

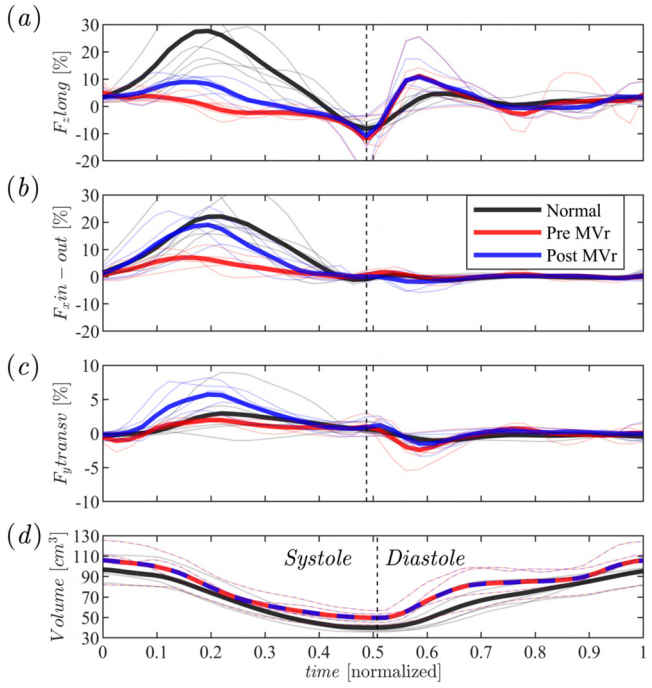

FIG. 10. Time course of the three components of the dimensionless hemodynamic force vector: *z* or longitudinal component (a), *x* or inlet-outlet component (b), and *y* or transversal component (c). The volume curve (d) is reported at the bottom for timing reference. Each curve represents the average computed from the cases of each group: normal (black lines) pre-MV_r (red), and post-MV_r (blue).

the vorticity curve after MV_r grows rapidly during the rapid filling phase[56] with E-wave peak being reached earlier due to a more vigorous jet. It also decays more rapidly during the diastasis phase due to the breaking down of the intense vortex pattern. This is confirmed by the curve in Fig. 9(b) indicating a higher level of kinetic energy in the repaired cases. Energy that rapidly decays after the rapid increase and a noticeable additional impulse during atrial contraction that is not present before repair; this can be important because the A-wave reflects blood flow from an active contraction.[57] Similarly, the kinetic energy dissipation, shown in 9 (*c*), is higher after repair during the early filling; however, it interesting to notice the higher dissipation before MV repair during the second part of diastole and onset of systole, the latter is likely imputable to the crossing going back to the insufficient MV for regurgitation. These evident differences observed during diastole are interesting because surgery is aimed to correct the insufficiency during systole; however, these results show how this correction to systole also affects diastole.

The energetic information reported above has an adjunct interpretation in terms of force exchanged between the blood and surrounding tissue. The three components of the dimensionless hemodynamic force vector are shown in Fig. 10. In normal cases the forces agree with what is reported in the clinical literature.[21,58,59] During systolic ejection the fluid is pushed toward the outflow tract along a predominantly longitudinal direction ($z-axis$) partly inclined along the inlet-outlet direction ($x-axis$) and negligible transverse component ($y-axis$) due to the approximate symmetry. After the systolic thrust, the force acts predominantly in the longitudinal direction [(10a)]: it reverses during the end of systole and at the onset of diastolic filling, first for the deceleration of outflow and then to acceleration of inflow, then it becomes positive again for the elastic resistance to LV filling at the end of E-wave.

The forces in pre-MV_r cases are very weak during systolic ejection, this is because of MV regurgitation into the atrium that reduces the momentum of the ejected flow and also induces a rotary movement with a deviated direction in the posterior ventricular tract [Fig. 8(e)]. Consequently, mitral regurgitation has a greater impact on the right section of the atrium (being P-type prolapses), providing important information on the phenomenon of the Coanda effect.[6,7,60] Post-MV_r shows a net improvement in systolic forces although it is interesting to emphasize the increase in all direction with an eventual modulus compared to normal; a potential sign of an effort by the LV to synchronize and redirect flow in a new direction. Of note, the surgical repair does not affect substantially the dynamic interaction during diastole.

An immediate perception of the spatial force distribution can be obtained by showing the polar histogram in Fig. 11 on the (x, z) plane. The normal cases feature the highest force directed toward aorta and smaller contributions in the diastolic phase. In pre-MV_r cases, as the flow is redirected both toward the LV outflow and the insufficient MV, hemodynamic force shows a dominance in the apex-base direction; this behavior is corrected in post-MV_r cases that show a significant redistribution toward a more physiological condition with inclined flow (in systole) and small vertical contribution (diastole).

B. Regurgitation and wash-out analysis

Before proceeding with the analysis of *MVr*, the flow transit results obtained for the normal cases with the method described in Sec. III B are preliminarily compared with those available in the literature in similar populations and obtained with phase-contrast MRI (known as "4D Flow MRI") with a different post-processing based on particle tracking.[34,61–64] The data reported in 4D Flow MRI literature can show a certain discrepancy when compared with the numerical method. The differences may be partly attributable to the simplifying assumptions present in the numerical model as well as in the different spatial resolution that in 4D Flow MRI (approximately 3 mm) is much smaller than the current numerical simulation (< 0.1 mm) or the

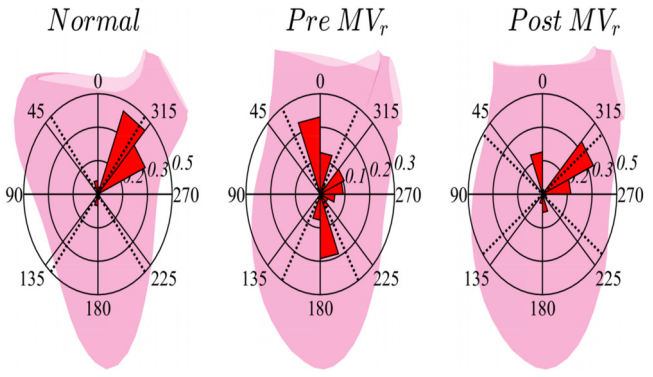

FIG. 11. Polar histogram of the angular frequency, in the (x, z) plane, of the hemodynamic force for the normal, pre- and post-MV_r cases.

TABLE III. Comparison of normal cases with 4D Flow MRI literature. EF is the ejection fraction, V_{direct} is the direct flow after on heartbeat, $V_{retained}$ is the retained volume after one heartbeat, $V_{delayed}$ is the delayed volume after one heartbeat, and $V_{residual}$ is the residual volume after one heartbeat.

	EF (%)	V_{direct} (%)	$V_{retained}$ (%)	$V_{delayed}$ (%)	$V_{residual}$ (%)
Normal	59	40	19	19	22
62	61	45	16	16	23
63	61	42	19	19	20
64	58	40	18	18	24
65	61	40	21	21	18

TABLE IV. Flow transit analysis in normal, pre- and post-MV_r cases. All volumes are normalized with EDV and represented in mean ± SD.

	EF (%)	V_{direct} (%)	$V_{retained}$ (%)	$V_{delayed}$ (%)	$V_{residual}$ (%)	V_{reg} (%)
Normal	59 ± 2	40 ± 3	19 ± 5	19 ± 5	22 ± 3	0
Pre-MV_r	53 ± 4	15 ± 8	23 ± 5	16 ± 5	24 ± 2	22 ± 4
Post-MV_r	53 ± 4	35 ± 4	21 ± 4	21 ± 3	22 ± 4	1 ± 1

different temporal resolution ($25 - 30$ ms vs < 0.1 ms), both calculations are also affected by the accuracy of the image post-processing. In addition, there is a systematic difference regarding first principles that requires a correction to allow a reliable comparison: the numerical model ensures the mass balance by construction; this is not always satisfied in 4D Flow MRI results that sometimes show differences between the measurements of the LV inflow (14) and outflow (16). This error can be corrected by simple redistribution of the difference to the different volumes as described in Ref. 20. Table III shows a comparison between the average transit properties in our healthy cases in comparison to those present in the literature obtained with 4D Flow MRI and corrected to ensure integral mass balance. Results present a substantial agreement and represent an indirect validation of the present analysis.

The results of flow transit before and after MV_r, with normal for reference, are reported numerically in Table IV; the same are shown in Fig. 12 with pie graphs for a more immediate visual appreciation. These results confirm the drastic reduction of the regurgitation after repair that confirms the efficacy of the surgical procedure aimed to reduce valvular insufficiency. After repair, the volume of blood that was previously regurgitated (V_{reg}) is now principally transferred into the V_{direct} indicating that flow previously going to the MV is redirected toward the aortic outlet. This is also significant from the point of view of blood stagnation since V_{reg} would then return to the LV increasing its residence time before entering the circulation,[2] which is a risk factor for thrombus formation, atrial fibrillation and stroke.[65]

VI. CONCLUSIONS

This study provided a validation for a dynamic MV model, for the numerical simulation of the flow in the LV, that is based on clinical images and that can be applied at the individual patient level in a clinical scenario. The clinical analysis through this numerical model showed that the valve movement is fundamentally driven by the transmitral flow rate, thus by the LV volume curve. The role of the elastic properties of the tissue is negligible to the valvular motion and it is primarily dictating the shape of the MV leaflets, which is obtained from patient-specific clinical images. This result is consistent with recent discoveries in the cardiovascular research confirming that any type of ventricular modification caused by inflammation can trigger an LV arrhythmogenic cascade in patients with mitral valve prolapse,[66] modifying its excursion (start-final shape). Improved understanding and modeling is fundamental given that the consequences can become important as in the case of degenerative prolapse, where by ventricular arrhythmia may lead to sudden cardiac death.[67]

This numerical model has been used to evaluate valve repair in patients with different types of valve prolapse allowing an in-depth evaluation of the hemodynamic changes after such intervention. Results confirm that successful MV_r corrects regurgitation and improves the fluid dynamics under several aspects; however, a normal physiological conditions is not fully restored and several differences remain. It is important to emphasize that, although the surgical repair aimes to correct MV regurgitation during systole, it also induces alteration to diastole that impacts the eventual LV function. LV wash-out is significantly improved which is mainly related to the volume of blood that was originally regurgitated in the atrium preoperatively, now being redirected toward the aorta following corrective MV_r surgery. In dynamic terms, the observed post-surgical flow pattern demonstrates energy and vorticity values that increase more quickly during early diastole due to the post-repair reduction of the mitral valve orifice. This results in a more compact diastolic vortex that restores vortex formation time to normal values. However, the post-vortex does not produce physiological intraventricular circulation and breaks down into a disturbed flow which is reflected in terms of kinetic energy through the mitral valve and its effective dissipation. A clear improvement in the

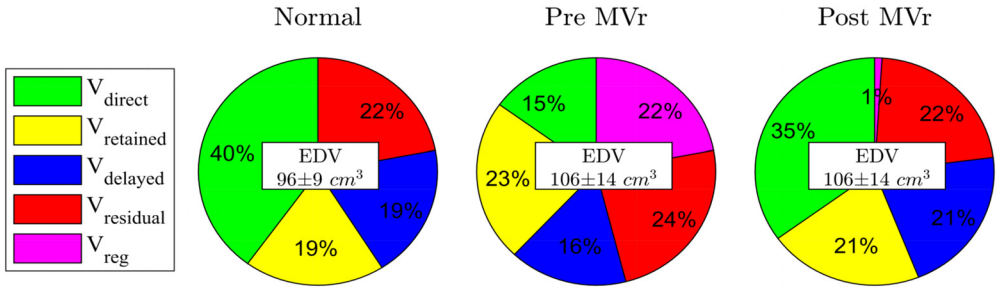

FIG. 12. Pie graphs of wash-out analysis in terms of mean value for normal pre- and post-MV_r cases.

HDF is observed which shows how the flow is undergoing a better thrust of the flow during the systolic phase, while the diastolic values remain apparently higher than normal.

This method offers optimal resolution and a level of computational detail for post-processing that would not be possible with other evaluation methods. An example is 4D Flow MRI which, on the one hand, would have the advantage of being an effective measurement on the patient, on the other hand, MRI having a low spatial and temporal resolution does not capture the small vortices that are very important for dispersion phenomena and that may not allow to identify in detail the actual distribution of the blood. In addition, the post-processing work of 4D Flow MRI data would be comparable to that required for a numerical simulation. The use of numerical simulations allows to obtain results with great detail and without additional examinations to the patient. Cardiac flow analysis allows to extend the knowledge on general clinical evaluation and cardiac surgery. A simple echocardiographic examination allows to obtain only basic information on the patient's health status, the evaluation in terms of energy, vorticity and HDF are parameters that to be calculated require sophisticated models such as the one proposed in this study.[18] The numerical model requires several hours of simulation but provides details and fundamental information for the study and evaluation of ventricular mechanics and, moreover, to define a full strategy on future valvular surgical modeling.

The evaluations made in this study are preliminary and have several limitations. The number of mechanical parameters of MV are approximated to obtain a purely diastolic fluid dynamic model, which includes the valve opening and closing process, while the solid model of MV deformation during systole is extremely approximate. The study sample size is limited and the analysis focused on the effect of geometric MV_r by assuming the same LV dynamics immediately after repair. Effective clinical results should consider the impact of surgical MV correction on left ventricular remodeling in a larger cohort over a longer follow-up period (3, 6, and 12 months). This is one of our objectives of currently ongoing studies.

Methodologically, our proposed model confirms the feasibility of an approach based on numerical models to integrate clinical imaging technology for the evaluation of various clinical scenarios. The same approach can be used to reproduce the virtual flow that would realize in diverse hypothetical hemodynamic conditions, therefore, introducing predictive capabilities to modern flow imaging technology.

ACKNOWLEDGMENTS

D.C., D.H.A., M.G.T., Z.A.F., and D.P. are supported by National Institutes of Health (NIH) grant 1R01HL166720-01A1 (M. G.T., Contact PI). G.P. is partially funded for this study by the Italian Ministry of Education and Research with grant: PRIN 2022AJT27Y, provided through the University of Trieste (CUP J53D23002030006).

AUTHOR DECLARATIONS

Conflict of Interest

Yes, D.H.A. is the National co-Principal Investigator for the Triluminate-II US Pivotal Trials, the Medtronic Apollo and CoreValve US Pivotal Trials, and ReChord US Pivotal Trial, respectively. The Icahn School of Medicine at Mount Sinai receives royalty payments from Edwards Lifesciences and Medtronic for intellectual property related to D.H.A.'s involvement in the development of 3 mitral valve repair rings and a tricuspid valve repair ring. DP received nonfinancial support from TOMTEC Imaging Systems GmbH (PI - research license for myocardial strain analysis software).GP is scientific consultant for Medis Medical Imaging (Leiden, NL).All other authors reported no conflicts of interest.

Ethics Approval

Ultrasound images were provided in anonymous form for post-processing in the context of a clinical study that was approved by the Institutional Review Board of the Icahn School of Medicine at Mount Sinai of New York, and all participants provided informed consent to the usage of data in anonymous form for scientific research.

Author Contributions

Dario Collia: Conceptualization (lead); Data curation (lead); Formal analysis (lead); Investigation (lead); Methodology (lead); Supervision (equal); Validation (equal); Writing – original draft (lead). **David H. Adams:** Conceptualization (lead); Data curation (equal); Investigation (equal); Supervision (equal). **Maria Giovanna Trivieri:** Data curation (supporting); Formal analysis (supporting); Investigation (supporting); Supervision (supporting). **Zahi A. Fayad:** Data curation (supporting); Investigation (supporting); Supervision (supporting). **Gianni Pedrizzetti:** Conceptualization (lead); Data curation (supporting); Investigation (equal); Methodology (equal); Supervision (supporting). **Dimosthenis Pandis:** Conceptualization (lead); Data curation (equal); Investigation (equal); Supervision (equal).

DATA AVAILABILITY

The data that support the findings of this study are available from the corresponding author upon reasonable request.

REFERENCES

[1]D. Oliveira, J. Srinivasan, D. Espino, K. Buchan, D. Dawson, and D. Shepherd, "Geometric description for the anatomy of the mitral valve: A review," J. Anat. **237**, 209–224 (2020).
[2]D. Collia, "Mitral valve asymmetry in healthy, pathological, and repaired cases," Phys. Fluids **22**, 077118 (2021).
[3]D. Collia and G. Pedrizzetti, "The influence of mitral valve asymmetry for an improved choice of valve repair or replacement," Fluids **7**, 293 (2022).
[4]J. E. Morningstar, C. Gensemer, R. Moore, D. Fulmer, T. C. Beck, C. Wang, K. Moore, L. Guo, F. Sieg, Y. Nagata, P. Bertrand, R. A. Spampinato, J. Glover, S. Poelzing, R. G. Gourdie, K. Watts, W. J. Richardson, R. A. Levine, M. A. Borger, and R. A. Norris, "Mitral valve prolapse induces regionalized myocardial fibrosis," J. Am. Heart Assoc. **10**, e022332 (2021).
[5]D. Collia, L. Zovatto, and G. Pedrizzetti, "Analysis of mitral valve regurgitation by computational fluid dynamics," APL Bioeng. **3**, 036105 (2019).
[6]D. Collia and G. Pedrizzetti, "Cardiac fluid dynamics in prolapsed and repaired mitral valve," in *Proceedings of XXIV AIMETA Conference 2019. AIMETA 2019, Lecture Notes in Mechanical Engineering*, edited by A. Carcaterra, A. Paolone, and G. Graziani (Springer, Cham, 2020), Vol. 1, pp. 857–867.
[7]D. Collia and G. Pedrizzetti, "Cardiac fluid dynamics of patient-specific geometries in pre and post mitral valve repair by direct numerical simulation," in *Seventh National Congress Of Bioengineering Proceeding. GNB 2020*, edited by A. Accardo, F. Brun, S. Marceglia, and G. Pedrizzetti (Pàtron Editor, 2020), Vol. 12, pp. 1–4.

[8]M. A. Miller, A. Devesa, P. M. Robson, S. L. Liao, R. Pyzik, A. El-Eshmawi, P. Boateng, D. Pandis, S. R. Dukkipati, V. Y. Reddy, D. H. Adams, Z. A. Fayad, and M. G. Trivieri, "Arrhythmic mitral valve prolapse with only mild or moderate mitral regurgitation," JACC Clin. Electrophysiol. **9**, 1709–1713 (2023).
[9]A. Carpentier, "Cardiac valve surgery–the French correction," J. Thorac. Cardiovasc. Surg. **86**, 323–337 (1983).
[10]D. H. Adams, R. Rosenhek, and V. Falk, "Degenerative mitral valve regurgitation: Best practice revolution," Eur. Heart J. **31**, 1958–1966 (2010).
[11]C. M. Otto, R. A. Nishimura, R. O. Bonow, B. A. Carabello, J. P. Erwin, III, F. Gentile, H. Jneid, E. V. Krieger, M. Mack, C. McLeod, P. T. O'Gara, V. H. Rigolin, T. M. Sundt, III, A. Thompson, and C. Toly, "2020 ACC/AHA guideline for the management of patients with valvular heart disease: A report of the American college of cardiology/American heart association joint committee on clinical practice guidelines," Circulation **77**, e25–e197 (2021).
[12]D. Collia, M. Vukicevic, V. Meschini, L. Zovatto, and G. Pedrizzetti, "Simplified mitral valve modeling for prospective clinical application of left ventricular fluid dynamics," J. Comput. Phys. **398**, 108895 (2019).
[13]V. Meschini, M. D. Tullio, G. Querzoli, and R. Verzicco, "Effects of natural and prosthetic mitral valves on the flow structure in healthy and pathological left ventricles," J. Fluid Mech. **834**, 271–307 (2018).
[14]F. Xu, S. Morganti, R. Zakerzadeh, D. Kamensky, F. Auricchio, A. Reali, T. Hughes, M. Sacks, and M. Hsu, "A framework for designing patient-specific bioprosthetic heart valves using immersogeometric fluid–structure interaction analysis," Int. J. Numer. Methods Biomed. Eng. **34**, e2938 (2018).
[15]N. Narula, N. Narula, and E. Argulian, "The thickened valve," JACC Case Rep. **2**, 1845–1848 (2020).
[16]C. Lee, R. Amini, S. Gorman, J. H. Gorman, III, and M. Sacks, "An inverse modeling approach for stress estimation in mitral valve anterior leaflet valvuloplasty for in-vivo valvular biomaterial assessment," J. Biomech. **47**, 2055–2063 (2014).
[17]F. Domenichini and G. Pedrizzetti, "Asymptotic model of fluid-tissue interaction for mitral valve dynamics," Cardiovasc. Eng. Technol. **6**, 95–104 (2015).
[18]D. Collia, E. Angeli, L. Careddu, and G. Pedrizzetti, "Analysis of the distribution and orientation of oxygenated and non-oxygenated blood in a double outlet right ventricle," Phys. Fluids **35**, 091905 (2023).
[19]D. Collia, L. Zovatto, G. Tonti, and G. Pedrizzetti, "Comparative analysis of right ventricle fluid dynamics," Front. Bioeng. Biotechnol. **9**, 667408 (2021).
[20]D. Collia, G. Libero, G. Pedrizzetti, and V. Ciriello, "Surrogate models provide new insights on metrics based on blood flow for the assessment of left ventricular function," Nat. Sci. Rep. **12**, 8695 (2022).
[21]D. Collia, G. Pedrizzetti, T. Sato, D. Matsubara, L. Zovatto, M. Gei, A. Banerjee, and G. Pedrizzetti, "Interplay between geometry, fluid dynamics, and structure in the ventricles of the human heart," Phys. Rev. Appl. **19**, 014006 (2023).
[22]C. Celotto, L. Zovatto, D. Collia, and G. Pedrizzetti, "Influence of mitral valve elasticity on flow development in the left ventricle," Eur. J. Mech./B Fluids **75**, 110–118 (2019).
[23]G. Faganello, D. Collia, L. Pagura, E. Croatto, L. M. Tosoni, P. Toritto, G. Pedrizzetti, and A. D. Lenarda, "Impact of left ventricular hemodynamic forces in adult patients with treated aortic coarctation and preserved left ventricular systolic function," Echocardiography **41**, e15742 (2024).
[24]G. Faganello, L. Pagura, D. Collia, G. Barbati, A. Paladino, M. D. Ferro, E. Croatto, G. Sinagra, G. Pedrizzetti, and A. D. Lenarda, "Prognostic value of echocardiographic evaluation of cardiac mechanics in patients with aortic stenosis and preserved left ventricular ejection fraction," Int. J. Cardiovasc. Imaging **39**, 565–574 (2022).
[25]O. Werner, D. Martins, F. Bertini, E. Bennati, D. Collia, I. Olivotto, G. Spaziani, A. E. Baruteau, G. Pedrizzetti, and F. Raimondi, "Comparative analysis of left ventricle function and deformation imaging in short and long axis plane in cardiac magnetic resonance imaging," Front. Cardiovasc. Med. **11**, 1388171 (2024).
[26]M. Dal Ferro, D. Stolfo, V. D. Paris, P. Lesizza, R. Korcova, D. Collia, G. Tonti, G. Sinagra, and G. Pedrizzetti, "Cardiac fluid dynamics meets deformation imaging," Cardiovasc. Ultrasound **16**(1), 10 (2018).
[27]H. T. Le, N. Hangiandreou, R. Timmerman, M. J. Rice, W. B. Smith, L. Deitte, and G. M. Janelle, "Imaging artifacts in echocardiography," Anesth. Analg. **122**, 633–646 (2016).
[28]F. F. Faletra, A. Ramamurthi, M. C. Dequarti, L. A. Leo, T. Moccetti, and N. Pandian, "Artifacts in three-dimensional transesophageal echocardiography," J. Am. Soc. Echocardiogr. **27**, 453–462 (2014).
[29]V. Meschini, M. D. Tullio, and R. Verzicco, "Effects of mitral chordae tendineae on the flow in the left heart ventricle," Eur. Phys. J. E **41**, 2–27 (2018).
[30]R. Ogden, *Non-Linear Elastic Deformations* (Dover, New York, 1997).
[31]A. E. Green and J. E. Adkins, *Large Elastic Deformations* (Clarendon Press, Oxford, 1960).
[32]J. H. Seo, V. Vedula, T. Abraham, A. C. Lardo, F. Dawoud, H. Luo, and R. Mittal, "Effect of the mitral valve on diastolic flow patterns," Biomech. Model. Mechanobiol. **26**, 121901 (2014).
[33]A. Bolger, E. Heiberg, M. Karlsson, L. Wigström, J. Engvall, A. Sigfridsson, T. Ebbers, J. P. E. Kvitting, C. J. Carlhäll, and B. Wranne, "Transit of blood flow through the human left ventricle mapped by cardiovascular magnetic resonance," J. Cardiovasc. Magn. Reson. **9**, 741–747 (2007).
[34]C. J. Carlhäll and A. Bolger, "Passing strange, flow in the failing ventricle," Circ. Heart Fail. **3**, 326–331 (2010).
[35]O. Prec, L. Katz, L. Sennett, R. Rosenman, A. P. Fishman, and W. Hwang, "Determination of kinetic energy of the heart in man," Am. Phys. Soc. **159**, 483–491 (1949).
[36]T. Hayashi, K. Itatani, R. Inuzuka, N. Shimizu, T. Shindo, Y. Hirata, and K. Miyaji, "Dissipative energy loss within the left ventricle detected by vector flow mapping in children: Normal values and effects of age and heart rate," J. Cardiol. **66**, 403–410 (2015).
[37]G. Pedrizzetti and P. P. Sengupta, "Vortex imaging: New information gain from tracking cardiac energy loss," Eur. Heart J., Cardiovasc. Imag. **16**, 719–720 (2015).
[38]W. Mawad, L. Løvstakken, S. Fadnes, T. Grønli, P. Segers, L. Mertens, and S. A. Nyrnes, "Right ventricular flow dynamics in dilated right ventricles: Energy loss estimation based on blood speckle tracking echocardiography - A pilot study in children," Ultrasound Med. Biol. **47**, 1514–1527 (2021).
[39]S. Frank, J. Lee, J. Lantz, T. Ebbers, and S. C. Shadden, "Cardiac kinetic energy and viscous dissipation rate from radial flow data," Front. Physiol. **12**, 725104 (2021).
[40]Z. Ashkir, S. Myerson, S. Neubauer, C. J. Carlhäll, T. Ebbers, and B. Raman, "Four-dimensional flow cardiac magnetic resonance assessment of left ventricular diastolic function," Front. Cardiovasc. Med. **9**, 866131 (2022).
[41]P. Kilner, G. Yang, A. Wilkes, R. Mohiaddin, D. Firmin, and M. Yacoub, "Asymmetric redirection of flow through the heart," Nature **404**, 759–761 (2000).
[42]A. Kheradvar, C. Rickers, D. Morisawa, M. Kim, G. Hong, and G. Pedrizzetti, "Diagnostic and prognostic significance of cardiovascular vortex formation," J. Cardiol. **74**, 403–411 (2019).
[43]A. Kheradvar, R. Assadi, A. Falahatpisheh, and P. P. Sengupta, "Assessment of transmitral vortex formation in patients with diastolic dysfunction," J. Am. Soc. Echocardiogr. **25**, 220–227 (2012).
[44]J. O. Mangual, E. Kraigher-Krainer, A. D. Luca, L. Toncelli, A. Shah, S. Solomon, G. Galanti, F. Domenichini, and G. Pedrizzetti, "Comparative numerical study on left ventricular fluid dynamics after dilated cardiomyopathy," J. Biomech. **46**, 1611–1617 (2013).
[45]J. R. Hove, R. W. Köster, A. Forouhar, G. Acevedo-Bolton, S. Fraser, and M. Gharib, "Intracardiac fluid forces are an essential epigenetic factor for embryonic cardiogenesis," Nature **421**, 172–177 (2003).
[46]P. M. Arvidsson, J. Töger, M. Carlsson, K. Steding-Ehrenborg, G. Pedrizzetti, E. Heiberg, and H. Arheden, "Left and right ventricular hemodynamic forces in healthy volunteers and elite athletes assessed with 4d flow magnetic resonance imaging," Am. J. Physiol. Heart Circ. Physiol. **312**, H314–H328 (2017).
[47]G. Pedrizzetti, "On the computation of hemodynamic forces in the heart chambers," Am. J. Physiol. Heart Circ. Physiol. **95**, 109323 (2019).
[48]F. Domenichini, "On the consistency of the direct forcing method in the fractional step solution of the Navier–Stokes equations," J. Comput. Phys. **227**, 6372–6384 (2008).
[49]L. Bennati, V. Giambruno, F. Renzi, V. D. Nicola, C. Maffeis, G. Puppini, G. B. Luciani, and C. Vergara, "Turbulent blood dynamics in the left heart in the presence of mitral regurgitation: A computational study based on multi-series cine-MRI," Biomech. Model. Mechanobiol. **22**, 1829–1846 (2023).

[50]A. Zingaro, I. Fumagalli, L. Dede, M. Fedele, P. C. Africa, A. F. Corno, and A. Quarteroni, "A geometric multiscale model for the numerical simulation of blood flow in the human left heart," Biomech. Model. Mechanobiol. **15**, 2391–2427 (2022).
[51]G. Pedrizzetti and F. Domenichini, "Left ventricular fluid mechanics: The long way from theoretical models to clinical applications," Ann. Biomed. Eng. **43**, 26–40 (2015).
[52]R. Mittal, J. H. Seo, V. Vedula, Y. J. Choi, H. Liu, H. H. Huang, S. Jain, L. Younes, T. Abraham, and R. T. George, "Computational modeling of cardiac hemodynamics: Current status and future outlook," J. Comput. Phys. **305**, 1065–1082 (2016).
[53]D. H. Adams, A. C. Anyanwu, P. B. Rahmanian, V. Abascal, S. P. Salzberg, and F. Filsoufi, "Large annuloplasty rings facilitate mitral valve repair in Barlow's disease," Ann. Thorac. Surg. **82**, 2096–2101 (2006).
[54]M. Daimon, S. Fukuda, D. H. Adams, P. M. McCarthy, A. M. Gillinov, A. Carpentier, F. Filsoufi, V. M. Abascal, V. H. Rigolin, S. Salzberg, M. L. A. Huskin, and T. Shiota, "Mitral valve repair with Carpentier-Mccarthy-Adams IMR ETlogix annuloplasty ring for ischemic mitral regurgitation: Early echocardiographic results from a multi-center study," Circulation **114**, 588–593 (2006).
[55]W. R. T. Witschey, D. Zhang, F. Contijoch, J. R. McGarvey, M. Lee, S. Takebayashi, C. Aoki, Y. Han, J. Han, A. J. Barker, J. J. Pilla, R. C. Gorman, and J. H. Gorman, "The influence of mitral annuloplasty on left ventricular flow dynamics," Ann. Thorac. Surg. **100**, 114–121 (2015).
[56]L. Bennati, G. Puppini, V. Giambruno, G. B. Luciani, and C. Vergara, "Image-based computational fluid dynamics to compare two mitral valve reparative techniques for the prolapse," bioRxiv **1**, 1–25 (2023).
[57]A. Demirkiran, M. E. C. J. Hassell, P. Garg, M. S. M. Elbaz, R. Delewi, J. P. Greenwood, J. J. P. amd, S. Plein, R. J. van der Geest, and R. Nijveldt, "Left ventricular four-dimensional blood flow distribution, energetics, and vorticity in chronic myocardial infarction patients with/without left ventricular thrombus," Eur. J. Radiol. **150**, 110233 (2022).
[58]F. Vallelonga, L. Airale, G. Tonti, E. Argulian, A. Milan, J. Narula, and G. Pedrizzetti, "Introduction to hemodynamic forces analysis: Moving into the new frontier of cardiac deformation analysis," J. Am. Heart Assoc. **10**, e023417 (2021).
[59]G. Faganello, D. Collia, S. Furlotti, L. Pagura, M. Zaccari, G. Pedrizzetti, and A. D. Lenarda, "A new integrated approach to cardiac mechanics: Reference values for normal left ventricle," Int. J. Cardiovasc. Imaging **36**, 2173–2175 (2020).
[60]Y. Wang, A. Quaini, S. Canic, M. Vukicevic, and S. H. Little, "3D experimental and computational analysis of eccentric mitral regurgitant jets in a mock imaging heart chamber," Cardiovasc. Eng. Technol. **8**, 419–438 (2017).
[61]J. Eriksson, P. Dyverfeldt, J. Engvall, A. F. Bolger, E. T, and C. J. Carlhäll, "Quantification of presystolic blood flow organization and energetics in the human left ventricle," Am. J. Physiol. Heart. Circ. Physiol. **300**, H2135–H2141 (2011).
[62]L. O. Karlsson, H. Erixon, T. Ebbers, A. Bolger, and C. J. Carlhäll, "Post-cardioversion improvement in LV function defined by 4D flow patterns and energetics in patients with atrial fibrillation," Front. Physiol. **10**, 659 (2019).
[63]J. Sundin, J. Engvall, E. Nylander, T. Ebbers, A. F. Bolger, and C. J. Carlhäll, "Improved efficiency of intraventricular blood flow transit under cardiac stress: A 4D flow dobutamine CMR study," Front. Cardiovasc. Med. **7**, 581495 (2020).
[64]H. Kim, H. Sheitt, S. B. Wilton, J. A. White, and J. Garcia, "Left ventricular flow distribution as a novel flow biomarker in atrial fibrillation," Front. Bioeng. Biotechnol. **9**, 725121 (2021).
[65]S. Bäck, I. Skoda, J. Lantz, L. Henriksson, L. O. Karlsson, A. Persson, C. J. Carlhäll, and T. Ebbers, "Elevated atrial blood stasis in paroxysmal atrial fibrillation during sinus rhythm: A patient-specific computational fluid dynamics study," Front. Cardiovasc. Med. **10**, 1219021 (2023).
[66]M. G. Trivieri, P. M. Robson, V. Vergani, G. LaRocca, A. M. Romero-Daza, R. Abgral, A. Devesa, L. D. Azoulay, N. A. Karakatsanis, A. Parikh, C. Panagiota, A. Palmisano, L. DePalo, H. L. Chang, J. H. Rothstein, R. A. Fayad, M. A. Miller, V. Fuster, J. Narula, M. R. Dweck, A. Morgenthau, A. Jacobi, M. Padilla, J. C. Kovacic, and Z. A. Fayad, "Hybrid magnetic resonance positron emission tomography is associated with cardiac-related outcomes in cardiac sarcoidosis," JACC Cardiovasc. Imaging **17**, 411–424 (2024).
[67]M. A. Miller, D. H. Adams, D. Pandis, P. M. Robson, A. Pawale, R. Pyzik, S. L. Liao, A. El-Eshmawi, P. Boateng, J. Garg, S. Waterford, M. M. Weiner, S. R. Dukkipati, V. Y. Reddy, Z. A. Fayad, and M. G. Trivieri, "Hybrid positron emission tomography/magnetic resonance imaging in arrhythmic mitral valve prolapse," JAMA Cardiol. **5**, 1000–1005 (2020).